ADVANCED FUNCTIONAL MATERIALS
www.afm-journal.de

CVD-Synthesized $CsAg_2I_3$ Single Crystals toward Polarization UV Photodetection and Anti-Counterfeiting Identification

Mengxin Yu, Yalin Zhai, Kai Xu, Ruijie Song, Peng Wan, Daning Shi, Caixia Kan, Xiaosheng Fang, and Mingming Jiang**

Low-dimensional ternary silver halide ($CsAg_2I_3$), an emerging inorganic lead-free perovskite, has garnered significant scientific attention due to its strong quantum confinement effects, wide bandgaps, non-toxicity, and others. However, the photophysical properties and optoelectronic performance of $CsAg_2I_3$ materials and devices are significantly compromised by crystal quality and defects arising from liquid-phase preparation. Herein, 1D $CsAg_2I_3$ single crystals newly grown by the chemical vapor deposition method are reported. These crystals display exceptional quality and stability over a 3-month period despite exposure to air and moisture. The high in-plane anisotropic structure, phonon vibrations, and refractive index of $CsAg_2I_3$ crystals are also experimentally elucidated. Polarization-sensitive ultraviolet photodetector based on the $CsAg_2I_3$ monocrystal features a responsivity of 139 mA W^{-1}, a specific detectivity of 1.05×10^{11} cm $Hz^{1/2}$ W^{-1}, an ultra-fast photoresponse speed of 48.2/69.1 µs, and a dichroic ratio of 2.66 upon 360 nm irradiation at −5.0 V bias. The photodetector excels amongst its competitors, moving toward the potential application of rapid optical anti-counterfeiting identification. This work, which leverages grown high-crystalline and highly stable $CsAg_2I_3$ monocrystals, holds promises for advancing this functional material into a robust next-generation optoelectronic devices capable of probing sensitive optical sensing and specific azimuth recognition.

1. Introduction

With the ever-increasing interest in metal halide perovskites (MHPs), these crystalline semiconductors are considered as potential candidates for developing multifunctional optoelectronic applications like solar cells, light-emitting diodes (LEDs), photodetectors (PDs), transistors, and more.[1–12] Among its huge potential in disruptive photoelectric technologies, MHP-based PDs find extensive use in optical communications, night vision, target detection, autonomous driving, and other fields, benefiting from high absorption coefficients, tunable band gaps, and versatile preparation procedures of high-quality monocrystalline materials.[13–17] Notable progress in the development of lead (Pb) halide perovskite-based PDs, the intrinsic toxicity of the heavy metal Pb in optoelectronic materials stifles their widespread application potential.[18–21] In this context, recent efforts have therefore explored environmentally friendly metal cations as substitutes for Pb^{2+}, including Sn^{2+}, Bi^{3+}, Sb^{3+}, Cu^{+}, and others.[22–24] Nevertheless, certain issues persist: 1) instability under conditions of moisture, heat, and light; 2) suboptimal optoelectronic properties for commercial products.[25,26] Consequently, the primary challenge remains to advance the exceptional optoelectronic properties and environmental stability of Pb-free perovskite alternatives.

Recently, there has been much research focused on Pb-free MHP materials to conquer the Pb-toxicity challenge.[27,28] Especially, a newly developed ternary silver halide perovskite has emerged as a research hotspot for applications in X-rays and UV detection due to its nontoxicity, strong quantum confinement effects, large band gap, outstanding stability, and other factors.[29–33] For instance, a highly stable UV PD has been created using the Pb-free perovskite $CsAg_2I_3$ monocrystal, renowned for its comprehensive stability, encompassing phase, optical, chemical, and thermal stability (up to 893 K).[31] An X-ray detector with high-resolution imaging capability has been fabricated based on a $CsAg_2I_3$ microbelt, demonstrating good flexibility across different bending radii and bending cycles.[32] Additionally, the

M. Yu, Y. Zhai, K. Xu, P. Wan, D. Shi, C. Kan, M. Jiang
College of Physics
MIIT Key Laboratory of Aerospace Information Materials and Physics Key Laboratory for Intelligent Nano Materials and Devices
Nanjing University of Aeronautics and Astronautics
Nanjing 211106, P. R. China
E-mail: mmjiang@nuaa.edu.cn

R. Song
School of Physics and Optoelectronic Engineering
Yangtze University
Jingzhou 434023, P. R. China

X. Fang
Department of Materials Science
State Key Laboratory of Molecular Engineering of Polymers
Fudan University
Shanghai 200433, P. R. China
E-mail: xshfang@fudan.edu.cn

The ORCID identification number(s) for the author(s) of this article can be found under https://doi.org/10.1002/adfm.202413903

DOI: 10.1002/adfm.202413903

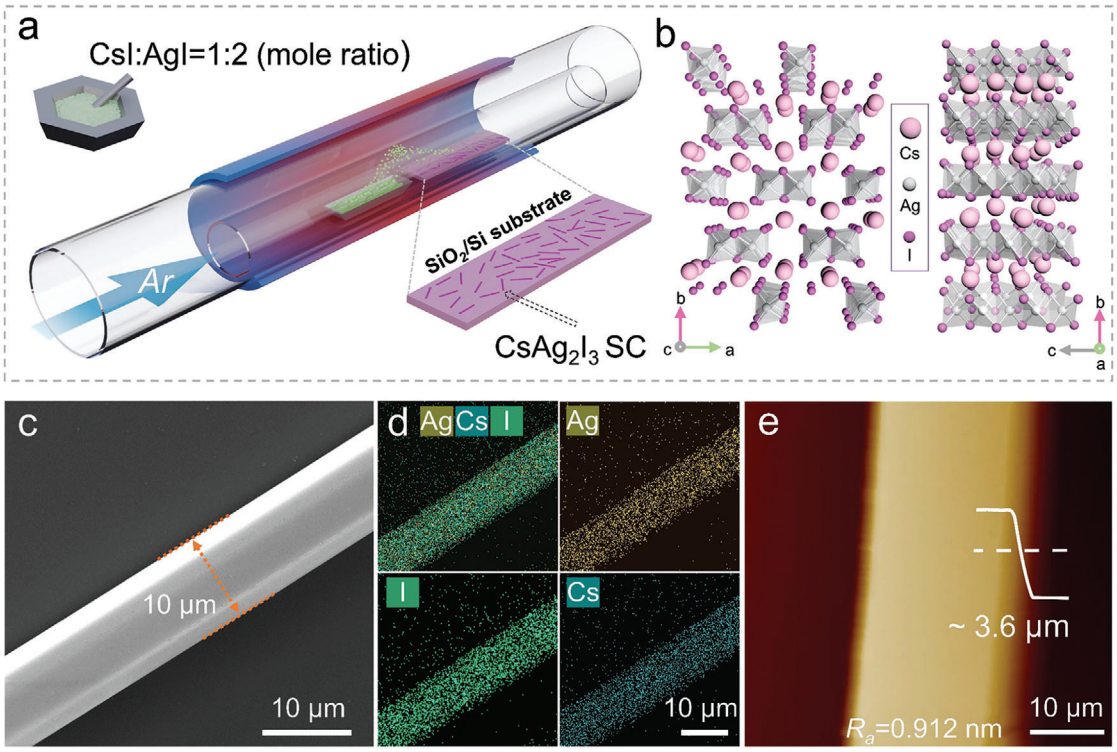

Figure 1. The growth and characterization of CVD-synthesized $CsAg_2I_3$ SCs. a) Growth illustration of individual $CsAg_2I_3$ SCs. b) Atomic structure of $CsAg_2I_3$ crystal viewed along the *c* and *a*-axis, respectively. c) A typical SEM observation of a $CsAg_2I_3$ SC. d) EDS mapping of the Cs, Ag, and I elements, which are distributed uniformly within the SC. e) AFM image and height measured on account of a $CsAg_2I_3$ SC.

$CsAg_2I_3$ film with highly transparent and stable performances has been utilized to construct self-powered visible-blind heterojunction PD toward potential commercial applications.[33] Despite continuous attempts on the MHPs-related materials and devices, which have revealed exciting and promising opportunities for optoelectronic fields, it is unsatisfactory that the photophysical properties and excellent performance observed in analogous structures have not been replicated in $CsAg_2I_3$.[34–36] At its root, $CsAg_2I_3$ has not yet fully met the needs of next-generation optoelectronic devices for practical applications due to the much-maligned liquid-phase growth process, which results in products with unstable grain boundaries susceptible to moisture, while retaining solvent residues.[37–41] Therefore, developing a robust and experimentally available scheme to prepare semiconductor monocrystals with highly-crystallized, phase purity, few grain boundaries, and defects is crucial for advancing material exploration and enhancing device performance.

Herein, 1D inorganic lead-free $CsAg_2I_3$ monocrystalline microrods have been successfully synthesized using a facile chemical vapor deposition (CVD) to the current acknowledgment. Comprehensive characterizations have revealed that the rod-like structures exhibit uniform and ordered structure crystals, along with intriguing optoelectronic properties and nonlinear/polarization optical features of the CVD-synthesized $CsAg_2I_3$ SCs. While owning wide bandgap energy, excellent photophysical characteristics, and structural/optical anisotropy, the $CsAg_2I_3$ SC emerged as an ideal candidate enables to the development of polarization-sensitive PD featuring in the UV spectra region. The device exhibits strong competitiveness, with its performing metrics including a responsivity of 139 mA W^{-1}, a specific detectivity of 1.05×10^{11} cm $Hz^{1/2}$ W^{-1}, an ultra-fast response speed of 48.2/69.1 μs and a large dichroic ratio of 2.66 upon 360 nm illumination at −5 V bias. Capitalizing on these significant photosensitive specialties, especially its ultrafast response speed, and capability to resolve linearly polarized light, the CVD-obtained $CsAg_2I_3$ SC PD held promise for applications in optical anti-counterfeiting recognition.

2. Results and Discussion

In this experiment, the synthesis procedure of 1D rod-like $CsAg_2I_3$ single crystals (SCs) via one-step CVD is schematically displayed in **Figure 1a**. Briefly, the samples of cesium iodide (CsI) and silver iodide (AgI) powders were used as the Cs, Ag, and I precursors, respectively. After mixed thoroughly, the precursor was positioned into a corundum boat. A freshly cleaned SiO_2/Si wafer, working as the growth substrate, was placed next to the corundum boat downstream of the protective argon (Ar) stream. The synthesis of $CsAg_2I_3$ SCs was performed at ≈650 °C with Ar as the carrier gas for 50 min. A comprehensive description of the growth process is available in the Experiment Section. To observe typically low-dimensional perovskite structure, top and side views of asymmetric $CsAg_2I_3$ crystalline structures are shown in Figure 1b, which are along the *c*-axis ([001]) and *a*-axis ([100]), respectively. The rod-like $CsAg_2I_3$ SC schematically exhibits an orthorhombic structure with unit cell lattice

constants: $a = 1.37432$ nm, $b = 0.62306$ nm, $c = 1.10763$ nm, $\alpha = \beta = \gamma = 90^{\circ}$; and belongs to space group *Pnma* (62). The lattice consists of chains of $[AgI_4]^{3-}$ tetrahedral units interconnected to each other along the [001], which are separated by adjacent Cs atoms, thus forming an approximate core–shell structure.[23,30] Two $[AgI_4]^{3-}$ tetrahedrons connecting allow to form a 2-fold chain by sharing the edge I atoms along the *a*-axis, resulting in the $[Ag_2I_6]^{4-}$ octahedron. These octahedral structures enable them to be bundled with each other in the *ab*-plane via Cs^+ cations. Note that the covalent bonds only exist along the 1D chains; as a result, the (001) plane has a higher surface energy than that of dangling bond-free (100) or (010), thereby being responsible for the rod-like shape growth along *c*-axis.[35] Consequently, this anisotropic crystal structure generates distinct space charge density distributions across various crystalline phases, enabling a differential response to polarized light in different directions. This characteristic opens up opportunities for designing PDs that are sensitive to polarized light. Furthermore, the pronounced 1D electronic structure of $CsAg_2I_3$ SCs facilitates efficient charge transport along the *c*-axis, which gives rise to rapid photoresponse.

The CVD-fabricated $CsAg_2I_3$ SC exhibits a rod-like morphology that appears translucent and colorless upon ambient light, as depicted in Figure S1, Supporting Information. In Figure 1c, a top-view scanning electron microscope (SEM) image of a $CsAg_2I_3$ SC reveals smooth side facets (the cross–section width of ≈10 µm) without prominent grain boundaries, suggesting favorable carrier transport features. Cross–sectional SEM image (Figure S2, Supporting Information) also shows no grain boundaries or voids in SCs, demonstrating excellent crystallinity. The elemental composition of a SC was quantitatively evaluated by energy dispersive spectroscopy (EDS) mapping. In which, Ag, Cs, and I elements are evenly distributed throughout the entire crystal, as shown in Figure 1d. In Figure S3, Supporting Information, the quantified atomic ratio of 1:2:3 for Cs:Ag:I consistent with the standard stoichiometry of $CsAg_2I_3$.[40] Furthermore, an atomic force microscopy (AFM) scan of the $CsAg_2I_3$ SC in Figure 1e shows that the SC has a height of ≈3.6 µm and a smooth upper surface. Note that it possesses a much lower root mean square (RMS) roughness of 0.912 nm compared to other previously reported perovskite SC films.[42,43] As discussed above, the CVD-synthesized $CsAg_2I_3$ SCs possess high-quality and smooth surfaces, making them well-suited for multifunctional optoelectronic applications.

To fully determine the electronic configurations of 1D $CsAg_2I_3$, we conducted calculations on its electronic band structure and density of states (DOS) using density functional theory (DFT). The outcomes, illustrated in Figure S4 in Supporting Information, reveal a direct bandgap of 3.45 eV at the G point, which is in accordance with previously reported literature.[31,32] The related DOS analysis shows that the conduction band minimum (CBM) and valence band maximum (VBM) of $CsAg_2I_3$ are primarily composed of I-5p, Ag-4d, Ag-5s, Ag-4p orbitals, respectively. Essentially, the electronic states in the energy band are mainly contributed by the $[Ag_2I_6]^{4-}_{\infty}$ octahedrons, with insignificant involvement of Cs^+ ions in both the CBM and VBM. The presence of the core–shell structure of $CsAg_2I_3$ induces the formation of self-trapped excitons, resulting in an observable large Stokes shift and broadband photoluminescence, as depicted in Figure S5, Supporting Information. This interesting deviation may be attributed to the Jahn-Teller effect.[35,36,44]

High-angle annular dark-field scanning transmission electron microscopy (HAADF-STEM) and X-ray diffraction (XRD) techniques were sequentially employed to examine the atomic structure and phase purity of 1D $CsAg_2I_3$ SCs. The STEM image in **Figure 2**a reveals the homogeneous, flat surface with a clear boundary of the 1D $CsAg_2I_3$ SC nanostructure. As shown in Figure 2b, an unambiguous lattice spacing of 0.287 nm is observed, which is assigned to the (330) plane of the $CsAg_2I_3$ crystal. Corresponding fast Fourier transform (FFT) diagrams collected from the specimen clearly show a single set of patterns, signifying that the CVD-obtained $CsAg_2I_3$ SCs are well-crystallized with a monocrystalline nature. The FFT pattern associated with low-magnification STEM image confirms that CVD-synthesized $CsAg_2I_3$ monocrystalline exhibits the anisotropic structure. $CsAg_2I_3$ tends to crystallize preferentially along specific crystallographic directions, resulting in the formation of rod-like structures with a 1D morphology. XRD-2θ patterns of as-synthesized SCs plotted in Figure 2c depict four narrow and sharp dominant peaks at 10.39°, 20.72°, 31.22°, and 41.97°, which are assigned to crystallographic planes (110), (220), (330) and (440), respectively. Analysis based on a standard phase card (PDF#No. 00-052-1049) determines that CVD-synthesized $CsAg_2I_3$ samples are phase-pure orthorhombic crystals, devoid of any impurity phases.

The optical properties of as-fabricated $CsAg_2I_3$ SCs were measured using micro-UV–Vis absorption spectroscopy. Illustration in Figure 2d, the strong absorbance peak appears as a broad band featuring in the UV spectral region, with a distinct absorbance edge arriving at ≈360 nm. The resulting Tauc plot, shown in the inset of Figure 2d, demonstrates that $CsAg_2I_3$ SC possesses a direct bandgap of ≈3.45 eV, which is consistent with earlier-mentioned calculation findings. X-ray photoelectron spectroscopy (XPS) was utilized to perform the chemical nature and valence state of $CsAg_2I_3$ SCs. The XPS survey spectrum is displayed in Figure 2e, in which the position of C 1s peak for the carbon element at 284.5 eV was used to calibrate the binding energies. From the spectrum, it clearly unveils the composition and bond states of Ag 3d, Cs 3d, and I 3d in samples. The two characteristic peaks at ≈368.1 and 374.1 eV are attributed to Ag $3d_{5/2}$ and Ag $3d_{3/2}$ (Figure 2f), respectively, which are consistent with the binding energy of Ag^+ core-level.[30,31] Besides, the illustration in Figure S6, Supporting Information, the 3d doublet observed in the iodine and cesium core-level spectra respectively corresponding to binding energies of I ($3d_{5/2}$ 619.1 eV, $3d_{3/2}$ 630.6 eV) and Cs ($3d_{5/2}$ 724.5 eV, $3d_{3/2}$ 738.5 eV), which match well with Cs^+ and I^-. The calculated atomic ratio of Cs:Ag:I was ≈1:1.9:3.1, which was derived from the element peak areas and sensitivity factor. All of these findings testify that the CVD-grown $CsAg_2I_3$ crystals are of high quality and phase-pure.

The $CsAg_2I_3$, a newly developed all-inorganic lead-free halide perovskite, remains largely unexplored in terms of its optical properties, including nonlinear and polarized optics. To evaluate its second harmonic generation (SHG) performance, a pulsed laser operating at a wavelength of 1064 nm was utilized as the pumping source. The emitted signals were then gathered using a back-reflection geometry in either a parallel or perpendicular configuration under a photon-counting manner. The relevant

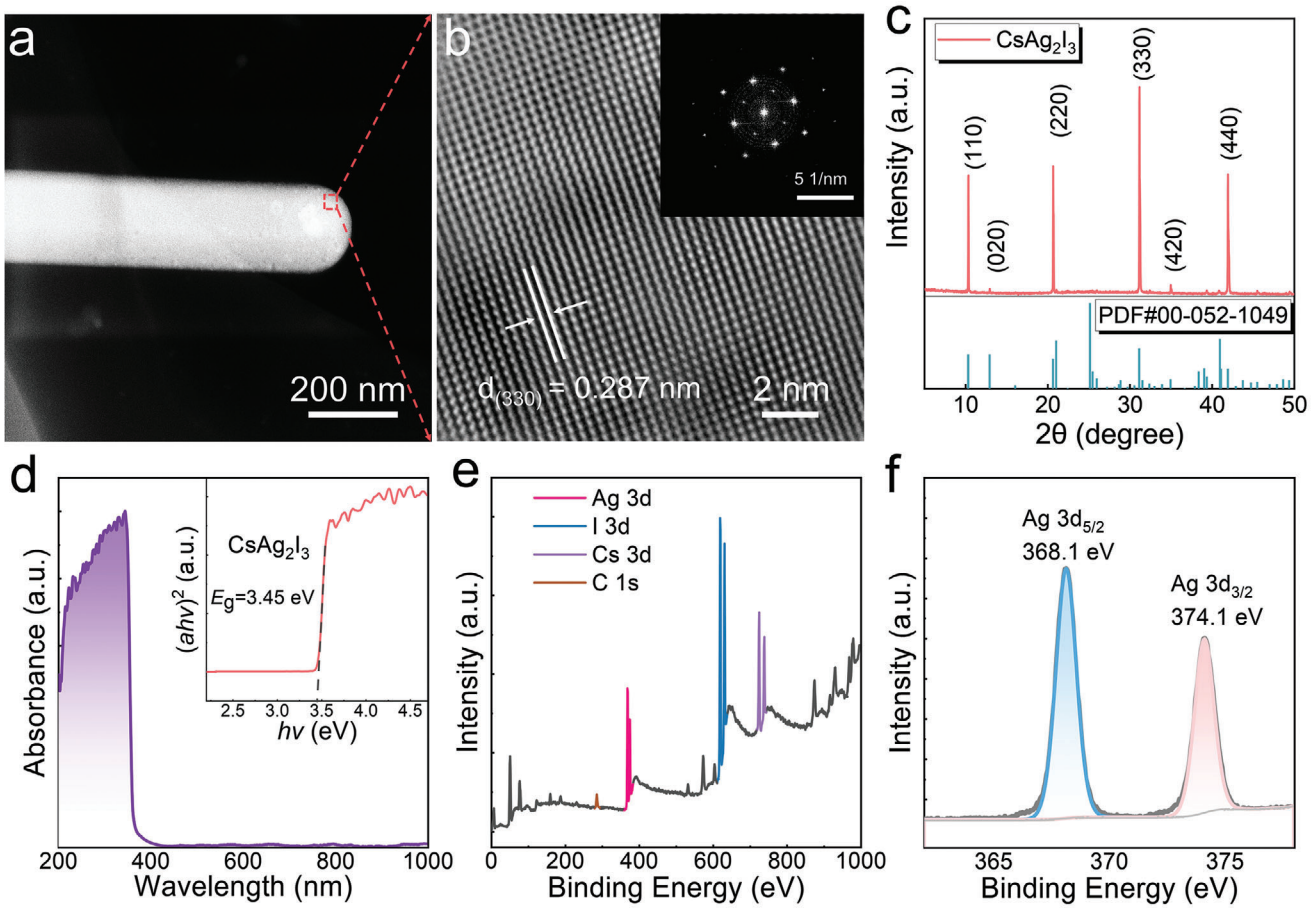

Figure 2. Characterizations of crystallographic structure, optical properties, and chemical nature of CVD-grown $CsAg_2I_3$ SCs. a) Low magnified HAADF-STEM of a small-size $CsAg_2I_3$ crystal. b) Atomic-resolution image and corresponding FFT pattern (up-right inset) of the sample as marked in a). c) XRD comparative diagram of $CsAg_2I_3$ SCs structure and standard phase. d) Steady-state absorption and extracted Tauc-curve (the inset) of the SC. e) XPS survey spectrum of CVD-synthesized $CsAg_2I_3$ SCs. f) Ag 3d XPS spectrum of the $CsAg_2I_3$ SCs.

schematic diagram of the SHG equipment is shown in **Figure** 3a. The target samples were positioned on a SiO_2/Si substrate, and a control reference experiment was conducted to eliminate the substrate as a potential source of SHG signal (Figure S7, Supporting Information). Figure 3b displays laser irradiance-dependent SHG spectra of $CsAg_2I_3$ SC with a peak at 532 nm, which belongs to the frequency doubling of the excitation laser resulting from the interaction between the incident photon and the $CsAg_2I_3$ sample. A power exponent of 1.67 was fitted for the relationship between SHG intensity and incident laser power, identifying the order of subsistent nonlinear process.[45] For $CsAg_2I_3$ crystals, which belong to centrosymmetric space groups, the observations of SHG can be interpreted as the symmetry breaking within the structure. This transition occurs from a highly symmetric form like tetrahedrons or octahedrons, to a low symmetric, distorted state. Such a phenomenon serves as a mechanism to maintain the minimum energy of the system, driven by the aforementioned Jahn-Teller effect.[36,46] Similar abnormal SHG signals have also been found in centrosymmetric materials, such as $PbBr_2$, $NbOCl_2$, $PdSe_2$, and $AsSbO_3$.[47–49] Additionally, the polarization-resolved SHG intensities were tested in the parallel and perpendicular configurations, as depicted in Figure 3c. Atomic anisotropic arrangement along various crystallographic directions influences the interaction probability between incident photons and the atoms. Consequently, certain directions demonstrate a higher probability of SHG, which is reflected in larger lobes within the polarization diagram. In contrast, smaller flaps are formed in other directions. The strong azimuthal dependence observed in the CVD-synthesized $CsAg_2I_3$ microrod is also evident in all enumerated materials, arises from in-plane anisotropy associated with symmetry breaking, which is well-proofed for the highly anisotropic crystal structure of $CsAg_2I_3$ SCs.

Apart from the SHG investigation, we have also conducted the angle-resolved polarization Raman spectroscopy (ARPRS), which allows to reveal the anisotropic phonon vibrational properties of $CsAg_2I_3$ SC. Using a 532 nm laser as the excitation source, we initially align the polarization direction parallel to the longer side of the $CsAg_2I_3$ SC, which designates this angle (θ) as 0°. In the measurement, the half-wave plate was rotated at a rate of 10° increments. Figure 3d,e illustrates 2D heat maps of wavenumber-dependent Raman intensities at various polarization angles (0 to 360°) in both parallel and perpendicular configurations. From the graphs, the vibrational intensity of the phonon modes, specifically for the I—Ag—I vibration at ≈110 cm^{-1}, demonstrates a

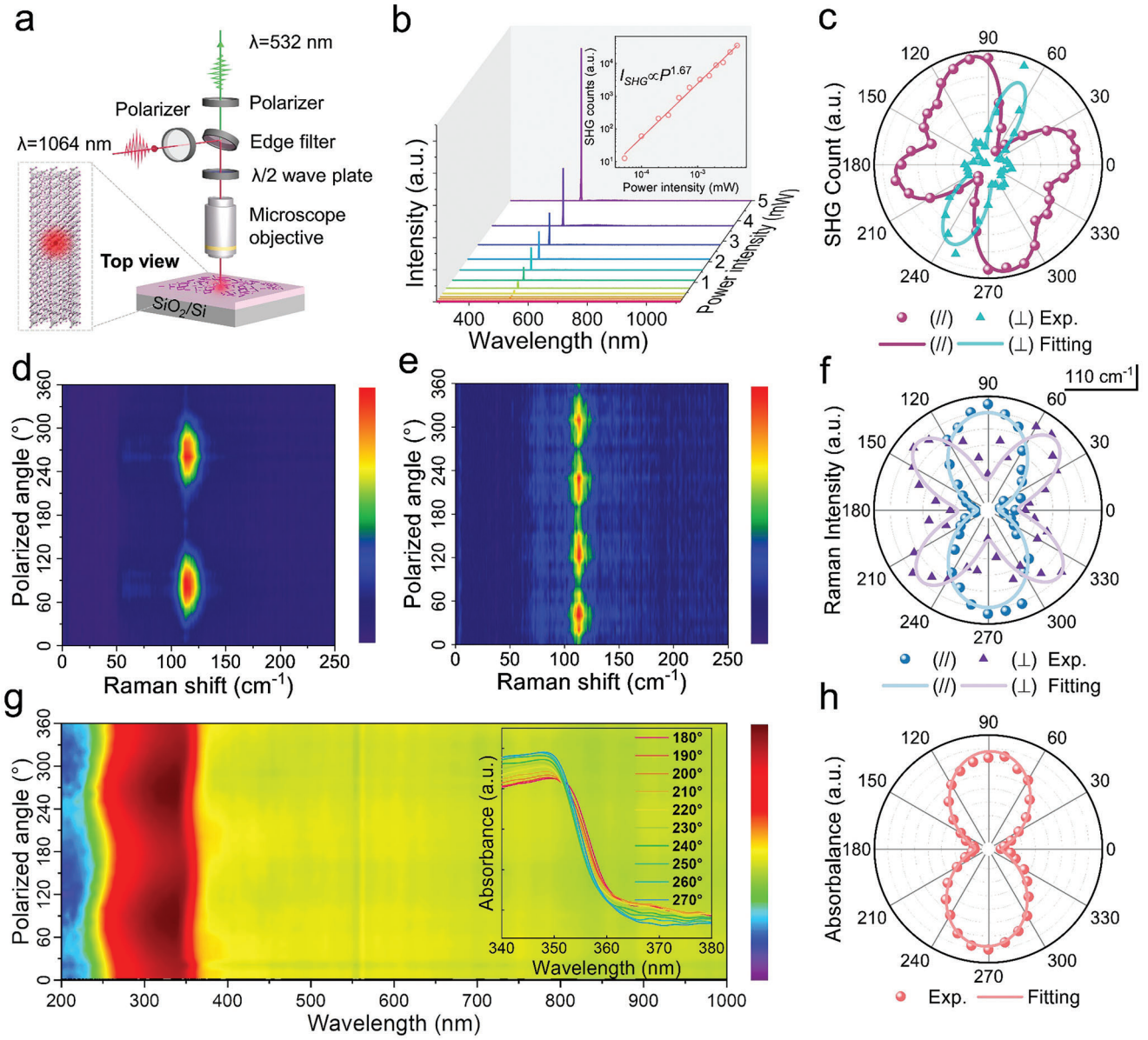

Figure 3. Optical anisotropy of a $CsAg_2I_3$ monocrystalline microrod. a) Schematic of a back-reflection SHG measurement setup. b) Power-dependent SHG spectra of a $CsAg_2I_3$ microrod (Pump laser source is 1064 nm). Inset: the linear fitting of SHG intensity overpowers density in a logarithmic manner, revealing a slope of ≈1.67. c) Angle-resolved polarized SHG spectra of $CsAg_2I_3$ SC measured in the parallel and perpendicular polarization configurations. d,e) Contour maps of ARPRS in the parallel and perpendicular polarization configurations, respectively. f) Polar plots of 110 cm^{-1} mode intensity in the parallel and perpendicular polarization configurations. g) Contour map of polarization-dependent UV–Vis absorption intensities of as-grown $CsAg_2I_3$ SCs. Inset: Angle-resolved absorption intensity curve from 340 nm to 380 nm, step: 10°. h) Polar plots of absorbance at a wavelength of 350 nm in the parallel polarization configurations.

notable periodicity with fluctuations of 180° (90°) as the polarization angle varies in parallel (perpendicular) configurations. In Figure 3f, the changes in Raman peak intensities versus polarization angles were also extracted and then plotted in polar coordinates. According to the selection rule, the Raman intensity (I) was determined using the function:[50]

$$I \propto \sum_j \left| e_i \times R_j \times e_s \right|^2 \quad (1)$$

where e_i, R_j, and e_s are the unit vector of incident radiation, the Raman tensor, and scattered radiation, respectively. The e_i and e_s are expressed as:

$$e_{i,\parallel} = e_{i,\perp} = \begin{pmatrix} \sin\theta & 0 & \cos\theta \end{pmatrix} \quad (2)$$

$$e_{s,\parallel} = \begin{pmatrix} \sin\theta \\ 0 \\ \cos\theta \end{pmatrix}, \; e_{s,\perp} = \begin{pmatrix} \cos\theta \\ 0 \\ -\sin\theta \end{pmatrix} \quad (3)$$

The Raman linear depolarization ratio (ρ) is defined as $\rho = I_{\perp}/I_{\parallel}$, where $I_{\perp}$ and $I_{\parallel}$ refers to the intensity of Raman scattered fields polarized orthogonally ($e_i \cdot e_s = 0$) and parallel ($e_i \cdot e_s = 1$) to the laser field polarization, respectively. Based on relevant group theory, the 110 cm^{-1} mode of $CsAg_2I_3$ has an extremely low depolarization ratio ($\rho = 0.23$), which is a feature of the A_g mode of $D_{2\ h}$ point group.[24,50] Raman tensor R_j can be written as follows:

$$R_j = \begin{pmatrix} a & 0 & 0 \\ 0 & a & 0 \\ 0 & 0 & b \end{pmatrix} \quad (4)$$

After matrix operations, the following calculation equations for 110 cm^{-1} in parallel and perpendicular polarization configurations are obtained:

$$I_{\parallel} \propto \left| a^2 \sin^2\theta + b^2 \cos^2\theta \right|^2 \quad (5)$$

$$I_{\perp} \propto \frac{|a-b|^2}{4} \sin^2 2\theta \quad (6)$$

This calculated vibration mode clearly reveals its polarization-sensitive characteristics, with well-fitted Raman intensities. In the parallel polarization configuration, the intensities exhibit a two-lobe shape, whereas in the perpendicular configuration, it shows a four-lobe shape. These findings once again confirm the pronounced in-plane structural anisotropy of 1D $CsAg_2I_3$ monocrystalline nano- and microstructures.

The asymmetric crystal structure of $CsAg_2I_3$ SC facilitates effective photon absorption with pronounced in-plane anisotropy.[34,51] In this case, the polarized angle-dependent optical absorption of $CsAg_2I_3$ SC was measured by a micro-absorption setup akin to the ARPRS equipment. The incident light signal is collected through both the crystal and the ultra-thin quartz substrate, with its initial polarization direction aligned parallel to the longer side of the crystal. Unlike the optical path used for polarization SHG and Raman testing setup, we have employed a dedicated transmission acquisition module for polarization absorption spectroscopy, as illustrated in Figure S8, Supporting Information. In the polarized absorption mapping displayed in Figure 3g, the sample was tested under parallel polarization configuration. The absorption spectrum experiences observable variations depending on the polarization angle of the incident light, with a periodicity of 180° in the UV spectral range. Absorption intensities at the minimum ($\theta = 0°/180°$) and maximum ($\theta = 90°/270°$) values are identified at 349 and 350 nm, respectively. The substantial attenuation of weak deep-UV light (≤250 nm) passing through the polarizer, crystal, and substrate sequentially, can cause its lower absorption intensity compared to visible light. Figure 3h illustrates the trend of absorbance versus the polarized light in polar plots. The in-plane anisotropy of optical absorption in a $CsAg_2I_3$ SC reflects the intrinsic refractive index variation of different crystal orientations.[51]

The extraordinary characteristics of $CsAg_2I_3$ monocrystalline microrods, which contain asymmetric crystal structure, anisotropic optical absorption, and ultra-wide bandgap, allow it as an ideal candidate for designing polarization-sensitive UV PDs. By transferring a microrod onto a SiO_2/Si substrate, we were able to fabricate a photodetection device with symmetric Au electrodes, as depicted in the schematic diagram of **Figure 4a**. An optical microscopic image of the device featuring a horizontal channel is provided in the inset of Figure 4a. Details regarding the fabrication and characterization processes are available in the Experimental Section. Notable that all fabrication and measurement processes were conducted under ambient conditions with a relative humidity of ≈35%. The output curves (I–V) under dark and light illumination by varying wavelengths are shown in Figure 4b, which reveal the sensitive photoresponse of the $CsAg_2I_3$ SC within the 320 to 400 nm range. The symmetrical nature of all curves indicates the photoconductive properties of the device and the presence of Ohmic contacts between $CsAg_2I_3$ and the Au electrodes. Moreover, the device yields an ultra-low dark current of 1.21×10^{-11} A at −5 V bias, suggesting its potential to obtain a low detection limit for UV light signals. Responsivity (R) and specific detectivity (D^*) representing the key indicators of a PD's photoresponse capability for UV light signals, are calculated as:[52,53]

$$R = \frac{I_{ph} - I_d}{PS} \quad (7)$$

$$D^* = \frac{R\sqrt{S\Delta f}}{I_n} \quad (8)$$

where I_{ph}, I_d, P, and S, Δf, I_n represent the photocurrent, dark current, optical irradiance, active area (6 μm^2), measurement bandwidth, and current noise, respectively. The spectral responsivity of $CsAg_2I_3$ SC-based PD measured ranging from 250 to 500 nm at −5 V bias, is plotted in Figure 4c. The R-curve unveils a prominent photoresponse (350 – 380 nm) with a full width at half-maximum of ≈22 nm, which enables our PD for specific wavelength photodetection in the UV spectral region. The maximum R of 46.3 mA W^{-1} is found at 360 nm, aligning with the wide optical bandgap of $CsAg_2I_3$. From Figure S9 (Supporting Information), the frequency-dependent noise current (I_n) of the device was dominated by flicker ($1/f$) and generated compound noise attributing to losses at the interface.[54] The ultra-low current noise of ≈1.02×10^{-13} A $Hz^{-1/2}$ at 1 Hz of our PD resulted in a maximum specific detectivity reaching ≈3.51×10^{10} cm $Hz^{1/2}$ W^{-1} at 360 nm, as detailed in Figure S10, Supporting Information.

By varying the light irradiances from 0.043 to 30.2 mW cm^{-2} of the incoming 360 nm LED, the photocurrent and dark current curves of the $CsAg_2I_3$ SC-based PD at −5 V are depicted in Figure 4d. Increasing illumination power density leads to a gradual rise in photocurrent value due to the generation of more electron–hole pairs within the illuminated $CsAg_2I_3$ channel. An evident different photoresponse is observed under UV light at various intensities, showcasing that the $CsAg_2I_3$ SC-based PD possesses significant capability to resolve light irradiance. Corresponding I-t characteristic curves of the $CsAg_2I_3$ SC-based PD in Figure 4e remain consistent photocurrent as the number of on-off switching cycles increases, indicating exceptional stability and reproducibility. The inset of Figure 4e shows the light irradiance-dependent photocurrent, the power law relationship between the I_{ph} and the P can be well fitted as $I_{ph} \propto P^{0.66}$, implying a complex process involving transport, trapping, and

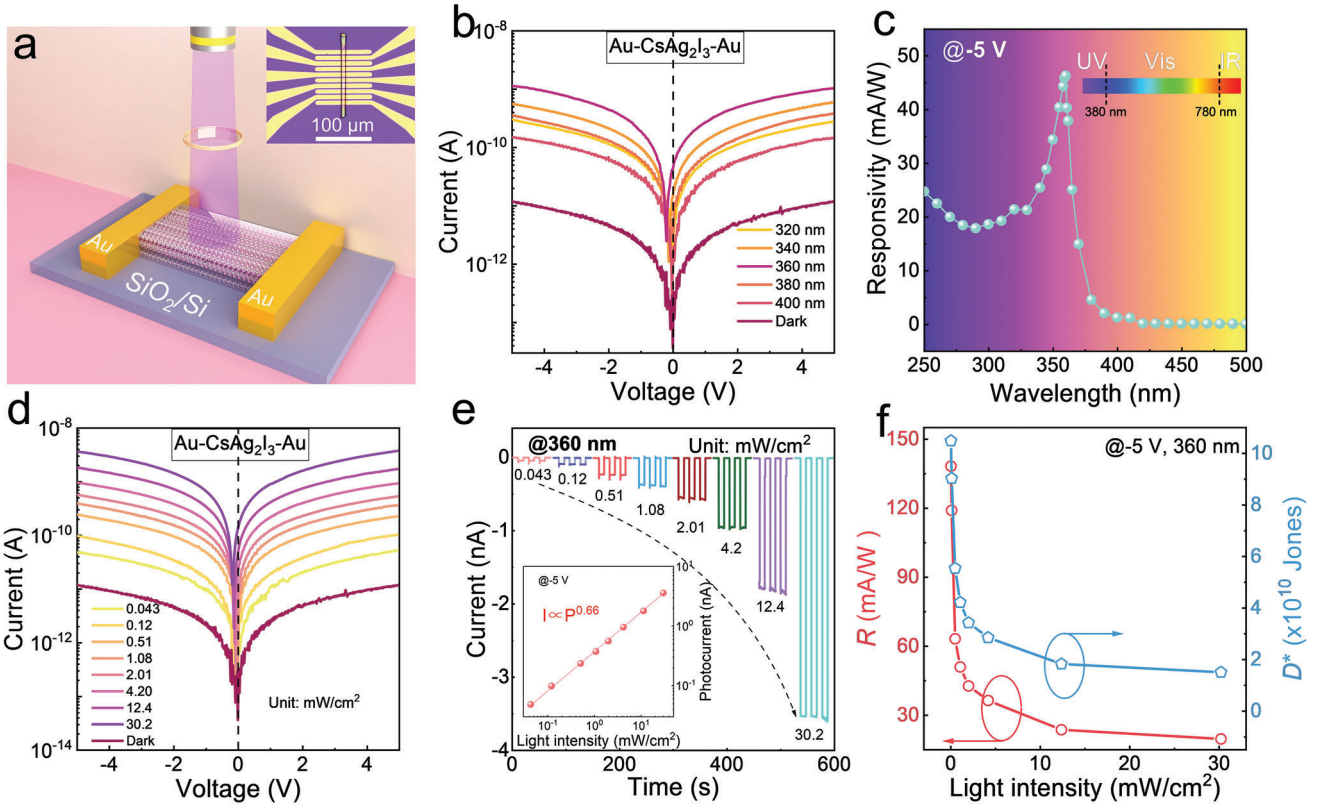

Figure 4. Photoresponse investigations of the designed $CsAg_2I_3$ SC-based PD. a) Schematic structure of an individual $CsAg_2I_3$ monocrystalline microrod photodetection device. Inset: optical image of the device. b) Wavelength-dependent *I–V* curves measured in the dark and under a consistent illumination power density. c) Wavelength-dependent *R* at −5 V bias. d) Light irradiance-dependent *I–V* curves upon 360 nm illumination. e) Light irradiance-dependent photocurrent upon 360 nm irradiation. Inset: The fitted relationship between photocurrent versus illumination power density. f) Light irradiance-dependent *R* and D^*.

recombination of the photo-generated carriers within the $CsAg_2I_3$ channel.[51] It is noted that pyroelectric-induced current spikes emerge at lower optical power densities but disappear at higher levels. The intriguing phenomenon occurs because the heat generated by intense light can disrupt the required temperature gradient for pyroelectric currents.[23,55] Moreover, the light irradiation power-dependent *R* and D^* at a wavelength of 360 nm were figured out. Given in Figure 4f, the maximum *R* and D^* reach up to 139 mA W^{-1}, 1.05×10^{11} cm $Hz^{1/2}$ W^{-1} under a light power intensity of 0.043 mW cm^{-2} at −5 V bias. Both the *R* and D^* values increase significantly with decreasing light irradiance, underscoring the device's ultra-sensitivity in detecting weak signals. Table S1 (Supporting Information) presents a performance comparison between our $CsAg_2I_3$ device and previous PDs constructed with $CsAg_2I_3$ that were grown using liquid-phase technologies. It is evident that the CVD-synthesized $CsAg_2I_3$ detector exhibits the most comprehensive performance, showcasing its potential for functional applications.

In **Figure** 5a, the fabricated $CsAg_2I_3$ SC-based PD enables it to achieve a stable operation upon 360 nm irradiation via 1.0 mW cm^{-2} at −5 V bias, which sustains 500 cycles without obvious deviation. It signifies the detector's robustness, reproducibility, and reliability at room temperature. This stable optoelectronic performance can be attributed to the high chemical stability of CVD-synthesized $CsAg_2I_3$ crystals. Notably, the XRD and XPS diffraction patterns of CVD-grown $CsAg_2I_3$ SC remain almost unchanged, with only slight changes in peak intensity observed from fresh samples to those aged for three months (Figure S11, Supporting Information). It indicates the robust stability of the crystalline structure of $CsAg_2I_3$ against UV radiation and environmental factors such as oxygen and moisture in ambient conditions (20 °C, ≈35% humidity). Additionally, a performance comparison of the $CsAg_2I_3$ PD, stored for 5 months, is detailed in Figure S12 of Supporting Information. The device can operate efficiently after being stored for three months without any packaging or protection, maintaining its performance without noticeable degradation under the same testing conditions.

The photoresponse speed, a critical figure-of-merit of our detector, indicates how quickly it responds to changes in light signals. The target device is exposed to a meticulously controlled 360 nm light source modulated at various frequencies, with data acquisition performed at a high sampling rate using a high-precision oscilloscope. Understanding its frequency-dependent response is essential for gathering crucial insights into its practical performance in real-world scenarios. Figure 5b displays the periodic photoresponse of $CsAg_2I_3$ SC-based PD at specific frequencies of 1, 5, 10, 50, 100, 500 Hz, 1, 5, and 10 kHz at −5 V bias. As the modulation frequency increased to 5 kHz, the PD's output waveform became less steep, yet remained free

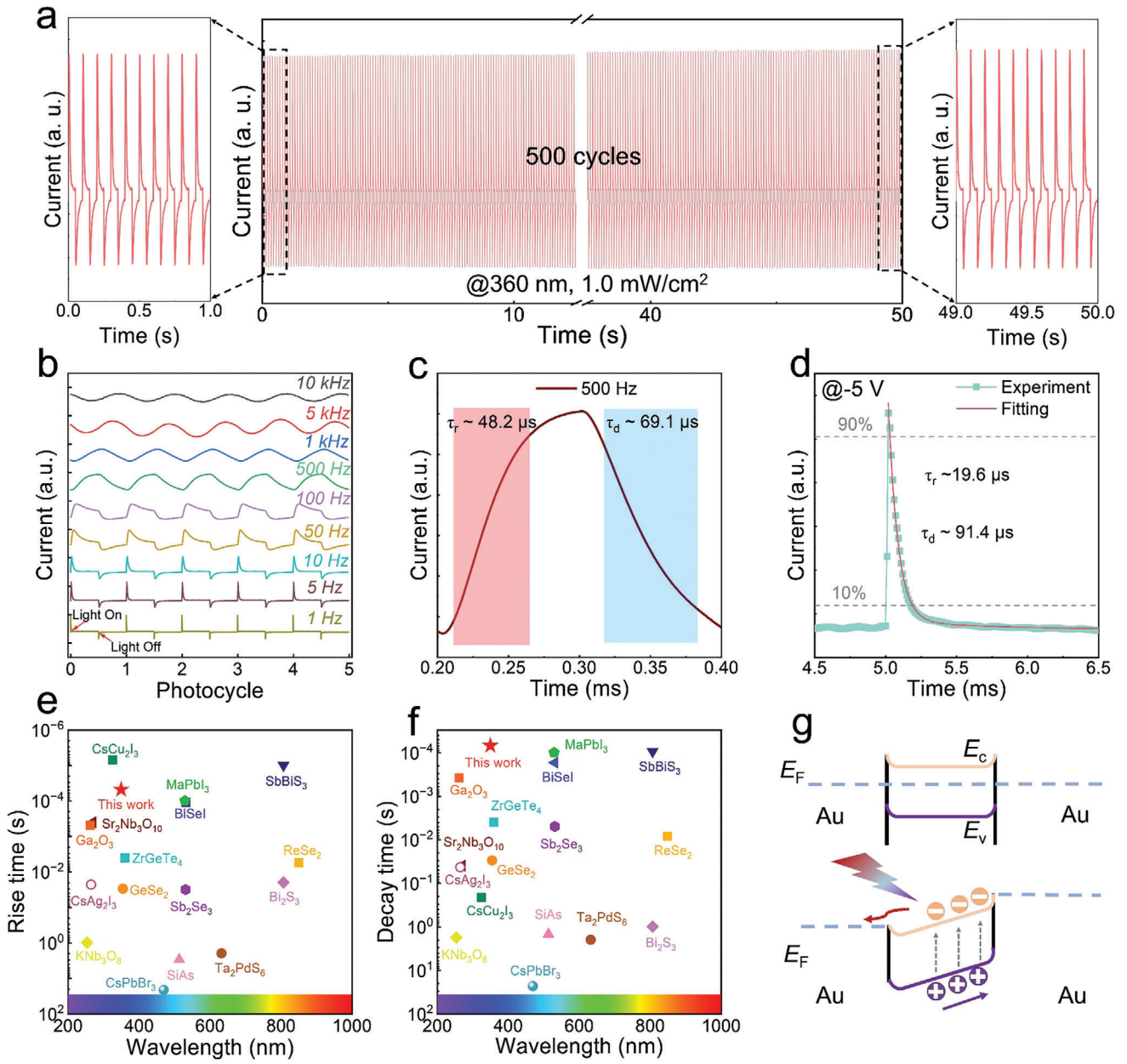

Figure 5. Photoresponse properties of the $CsAg_2I_3$ SC-based PD. a) Periodic photocurrent response under 1.0 mW cm^{-2} power intensity for 500 photoswitching cycles. b) Variable frequency-dependent transient photoresponse curves. c) An enlarged normalized cycle at 500 Hz to access the rise/fall time of the detector. d) Photoresponse speed of the device when exposed to a 360 nm pulse laser at 500 Hz. e,f) Summary of rise and decay times of the related PDs. g) Energy band diagram of the photoconductive PD at −5 V bias.

from noticeable distortion. Remarkably, even at high modulation frequencies such as 10 kHz, the device exhibited consistent light-switching behavior with exceptional reproducibility. Subsequently, by analyzing the photoresponse curve at 500 Hz, the response speed of the detector was estimated. Figure 5c presents the rise and fall times calculated to be 48.2/69.1 μs. These durations signify the transition photoresponse time of the PD to shift between 10% and 90%, and vice versa, of its peak value. Furthermore, the transient response of the detector was assessed using a high-precision oscilloscope with a pulsed nanosecond laser (360 nm, 500 Hz), as shown in Figure 5d. The pulse signal exhibits a rapid rise/fall time of 19.6/91.4 μs, which could be clearly distinguished. This speed is notably faster, by 2–3 orders of magnitude, compared to previously reported PDs based on liquid growth $CsAg_2I_3$.[30–33] Benefiting from the superior crystalline quality and efficient 1D charge transport channel of the CVD-synthesized $CsAg_2I_3$ monocrystalline microrods, the developed UV PD exhibits a faster response by comparing to mostly based on those 1D material systems and all reported Ag-based perovskite PD (Figure 5e,f), highlighting the potential

applications of CVD-grown $CsAg_2I_3$ PDs in the field of rapid UV detection.[20,21,24]

To systematically study the working mechanism of the $CsAg_2I_3$ SC-based PD, we illustrate the restructuring of the energy bands in Figure 5g by combining the optical bandgap with UV photoelectron spectroscopy (UPS) results (Figure S13, Supporting Information). The work function of Au is extracted to be ≈5.1 eV; while the conduction band (E_c), valence band (E_v) and Fermi level (E_F) of $CsAg_2I_3$ are ≈3.89, 7.34, and 4.86 eV, respectively. When our PD is illuminated by photons with an energy larger than the bandgap of $CsAg_2I_3$ (3.45 eV), electron–hole pairs will be created within the $CsAg_2I_3$ photoactive layer on account of the photoconductive effect. Driven by the biased voltage, the photoinduced electron–hole pairs undergo rapid separation, transport, and subsequent collection by the opposite Au electrode, thus resulting in the generation of photocurrent in an external circuit.

Our high-quality $CsAg_2I_3$ SCs are fabricated not only for ultrafast UV PDs but also for direct polarization-sensitive detection, representing a novel attempt based on inorganic silver halide perovskites. A polarization photocurrent test was established to investigate the linear dichroism of the $CsAg_2I_3$ SC-based PD. By switching the on–off state of the light (360 nm, 1.80 mW cm^{-2}) and synchronously rotating the angle of the half-wave plate with a step of 30° from 0° to 360° at the bias of −5 V, we continuously recorded the dynamic photoresponse of the $CsAg_2I_3$ SC-based PD. As anticipated, in **Figure 6a**, the PD exhibits an obvious photoresponse with a period of 180°, where the highest and lowest photocurrent were captured under the parallel and perpendicular configurations to the long side of $CsAg_2I_3$ crystalline, respectively. In general, the linearly polarized photocurrent is extracted and then fitted by the following formula:[6]

$$I_{ph} = I_{phmax}\cos^2\theta + I_{phmin}\sin^2\theta \quad (9)$$

where I_{phmax} and I_{phmin} are the maximum (0.606 nA) and minimum photocurrent (0.227 nA), respectively. Figure 6b shows that the fitted curve exhibits a gourd-like double flap shape in polar coordinates, owing to the structure and optical anisotropy of $CsAg_2I_3$ SCs. The device demonstrates a large anisotropic ratio (I_{phmax}/I_{phmin}) of ≈2.66 upon 360 nm illumination, which is competitive among the reported polarization-sensitive PDs in the UV spectral region.

Polarization optical anti-counterfeiting technology has been crucially employed in down-to-earth use by modern institutions worldwide, such as the perspective windows on Australian banknotes.[56] Drawing inspiration from this, we integrated a PD to implement polarization-based optical anti-counterfeiting measures, as depicted in Figure 6c. In the system, a 360 nm LED serves as the light source, and the light path is equipped without other optical accessories. The light vertically passes through the designed pattern for recognition, and the light signal is ultimately collected by our $CsAg_2I_3$ SC-based PD. The designed anti-counterfeiting pattern consists of a 1 × 1 cm^2 polarization film, which at the letter "Y" are all oriented horizontally and the rest vertically with respect to the optical axis. In the left image of Figure 6d, the pattern photo under ambient light is imperceptible to the naked eye. Superimposed light of the same polarization direction can pass through, whereas the polarized light in orthogonal directions will block or weaken each other. Only by covering the camera lens with horizontal and vertical polarization films along the optical axis, the transparent or black letter "Y" images can be captured, respectively (the right side of Figure 6d). Subsequently, in Figure 6e, the pattern's movement, with a step of 1 cm, is controlled by a stepper motor. The system operates by moving horizontally (x) and vertically (y) until all polarizer units within the anti-counterfeiting pattern have been scanned. The gathered photocurrent data are summarized and visually represented via rapid scanning, enabling successful analysis of anti-counterfeiting images while identifying the polarization direction of the light source. Considering the outstanding photostability and favorable biocompatibility of the $CsAg_2I_3$ SCs, we anticipate that this polarization-sensitive PD holds great potential for a wide range of advanced anti-counterfeiting applications, encompassing but not limited to information encryption, data storage, and other optoelectronic devices.

3. Conclusion

In summary, a green and efficient catalyst-free strategy is developed toward the one-step synthesis of large-scale 1D $CsAg_2I_3$ micron-ordered crystals via a facile CVD. Through theoretical calculation and experimental characterizations, the high-quality 1D $CsAg_2I_3$ SCs exhibit smooth morphology, pure phase composition, high UV absorption, and long-term environmental stability. Intriguingly, it is discovered that the $CsAg_2I_3$ SCs exhibit strong in-plane anisotropy in nonlinear optics, Raman vibration, and photon absorption across multispectral tests. Ultrawide bandgap (≈3.45 eV) enables $CsAg_2I_3$ monocrystalline structures optoelectronic devices to work well in the UV spectral region, showing the R of 139 mA W^{-1}, D^* of 1.05 × 10^{11} cm $Hz^{1/2}$ W^{-1} and an ultra-fast photoresponse speed ≈48.2/69.1 µs. On this basis, a polarization resolution photocurrent with a dichroic ratio of 2.66 in our PD at 360 nm is obtained. Moreover, these outstanding photosensitive properties of $CsAg_2I_3$ SC-PD jointly facilitate the achievement of fast optical anti-counterfeiting identification applications. This work, by employing high-quality growth approaches and systematic investigations on $CsAg_2I_3$ perovskite crystals, is anticipated to advance this functional material toward a robust optoelectronic device, thereby clarifying complex crystal structures, exploring new traits, and opening up multifunctional applications.

4. Experimental Section

Growth of 1D $CsAg_2I_3$ SCs: High-quality $CsAg_2I_3$ SCs were synthesized using one-step CVD in a high-temperature horizontal tube furnace. In brief, stoichiometric amounts of CsI (Aladdin, 99.99%) and silver iodide AgI (Aladdin, 99.99%) powders with a definite ratio of 1:2, were mixed and ground onto corundum boat in the middle of a vacuum quartz tube. Prior to heating, high purity Ar, as carrier gas (200 sccm), was used to purge oxygen from the furnace at a pressure of $<10^{-1}$ Pa. The silicon wafer was subjected to ultrasonic cleaning in a sequential manner using deionized water, acetone, ethanol, and deionized water again, with each cleaning step lasting 10 min. The cleaned wafer was dried with N_2 and set aside for later use. The furnace was then heated to 650 °C and held at this temperature

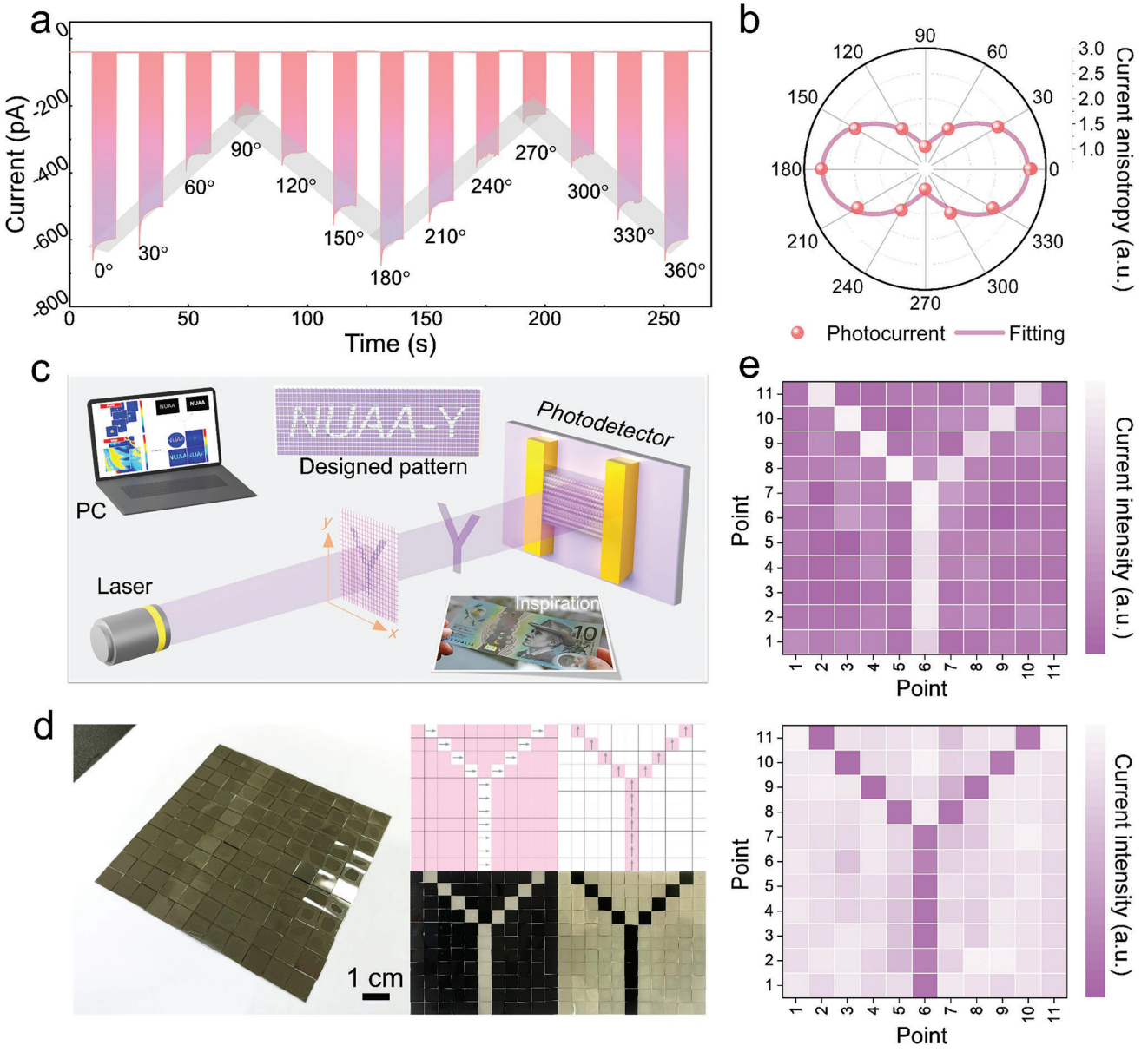

Figure 6. Polarization photodetection and optical anti-counterfeiting recognition application measurements based on the $CsAg_2I_3$ SC PD. a) Time-resolved polarized optoelectronic response of $CsAg_2I_3$ SC detector under the illumination of a linearly polarized 360 nm laser with a constant light irradiance of 1.80 mW cm^{-2} by varying the polarization angles. b) The angle-resolved photocurrent and fitted curve in polar coordinate. c) Schematic diagram of experimental setup through the integrated detector for anti-counterfeiting identification. d) Left: Anti-counterfeiting pattern upon an ambient light illumination. Right: Patterns captured with horizontal and vertical polarization lenses. e) The obtained 2D block heat mapping of text "Y" produced by PD via horizontal and vertical linear polarization 360 nm light.

for 50 min. The clean silicon wafer was placed next to the precursor source along the carrier gas direction as the growth substrate. After that, the furnace was cooled to room temperature naturally. The product of inorganic wide bandgap 1D $CsAg_2I_3$ crystals with high quality can be finally obtained on the substrate.

Characterizations: The synthesized samples were respectively characterized by an AFM (Bruker Dimension Edge), and a STEM (Talos F200s, Thermo Fisher). The surface morphologies and element composition of $CsAg_2I_3$ SC were characterized using SEM (TESCAN LYRA3 GM) and EDS, respectively. The crystal structure of the samples was tested using XRD (X'Pert3 Powder). The electronic structure and energy levels were carried out using XPS (ESCALAB Xi+, Thermo Scientific), and UPS radiation was generated by a He-gas discharge lamp (photon energy = 21.22 eV). The optical properties of an individual SC were tested by Raman spectroscopy and micro-UV–Vis spectrophotometer (ScanPro Advance, Metatest). Photoluminescence (PL) measurements of SCs were carried out by using a He—Cd laser as the excitation source (≈325 nm). The photoelectrical properties and photoresponse performances of the $CsAg_2I_3$ SC-based PD were characterized using a scanning photoelectric test system (MStarter 200). The response times of the device were measured by a system containing a pulse laser and an oscilloscope.

Supporting Information

Supporting Information is available from the Wiley Online Library or from the author.

Acknowledgements

This work was supported by the National Natural Science Foundation of China (No. 12374257) and the Postgraduate Research & Practice Innovation Program of NUAA (xcxjh20232106). The authors acknowledge the facilities in the Center for Microscopy and Analysis at Nanjing University of Aeronautics and Astronautics.

Conflict of Interest

The authors declare no conflict of interest.

Data Availability Statement

The data that support the findings of this study are available in the supplementary material of this article.

Keywords

anisotropy, anti-counterfeiting identification, $CsAg_2I_3$, polarization sensitives, UV photodetectors

Received: August 1, 2024
Revised: October 2, 2024
Published online:

[1] S. Sidhik, I. Metcalf, W. Li, T. Kodalle, C. J. Dolan, M. Khalili, J. Hou, F. Mandani, A. Torma, H. Zhang, R. Garai, J. Persaud, A. Marciel, I. A. M. Puente, G. N. M. Reddy, A. Balvanz, M. A. Alam, C. Katan, E. Tsai, D. Ginger, D. P. Fenning, M. G. Kanatzidis, C. M. Sutter-Fella, J. Even, A. D. Mohite, *Science* **2024**, *384*, 1227.
[2] L. Kong, Y. Sun, B. Zhao, K. Ji, J. Feng, J. Dong, Y. Wang, Z. Liu, S. Maqbool, Y. Li, Y. Yang, L. Dai, W. Lee, C. Cho, S. D. Stranks, R. H. Friend, N. Wang, N. C. Greenham, X. Yang, *Nature* **2024**, *631*, 73.
[3] A. Liu, H. Zhu, S. Bai, Y. Reo, M. Caironi, A. Petrozza, L. Dou, Y. Noh, *Nat. Electron.* **2023**, *6*, 559.
[4] G. Getachew, A. Wibrianto, A. S. Rasal, S. Kizhepat, W. B. Direrssa, V. Gurav, J. Chang, *Prog. Mater. Sci.* **2023**, *140*, 101192.
[5] J. Yang, F. Zhang, H. Xiao, Z. Wang, P. Xie, Z. Feng, J. Wang, J. Mao, Y. Zhou, S. Han, *ACS Nano* **2022**, *16*, 21324.
[6] X. Wang, Y. Wang, W. Gao, L. Song, C. Ran, Y. Chen, W. Huang, *Adv. Mater* **2021**, *33*, 2003615.
[7] D. Zhang, M. Zhu, Y. He, Q. Cao, Y. Gao, H. Li, G. Lu, Q. Cui, Y. Shen, H. He, X. Dai, Z. Ye, *Light: Sci. Appl.* **2024**, *13*, 82.
[8] Y. Hu, Z. Li, X. S. Fang, *J. Inorg. Mater.* **2023**, *38*, 1055.
[9] C. Zhou, W. Meng, L. Kong, C. Zhang, J. Zhang, F. Liu, H. Li, G. Jia, X. Yang, *Adv. Funct. Mater.* **2024**, *34*, 2307682.
[10] L. Zhang, L. Mei, K. Wang, Y. Lv, S. Zhang, Y. Lian, X. Liu, Z. Ma, G. Xiao, Q. Liu, S. Zhai, S. Zhang, G. Liu, L. Yuan, B. Guo, Z. Chen, K. Wei, A. Liu, S. Yue, G. Niu, X. Pan, J. Sun, Y. Hua, W.-Q. Wu, D. Di, B. Zhao, J. Tian, Z. Wang, Y. Yang, L. Chu, et al., *Nano-Micro Lett.* **2023**, *15*, 177.
[11] X. Pan, L. Ding, *J. Semicond.* **2022**, *43*, 020203.
[12] C. Li, Y. Ma, Y. Xiao, L. Shen, L. Ding, *InfoMat* **2020**, *2*, 1247.
[13] J. Sun, L. Ding, *Small* **2024**, *20*, 2308583.
[14] X. Feng, C. Li, J. Song, Y. He, W. Qu, W. Li, K. Guo, L. Liu, B. Yang, H. Wei, *Nat. Commun.* **2024**, *15*, 577.
[15] A. Morteza Najarian, M. Vafaie, A. Johnston, T. Zhu, M. Wei, M. I. Saidaminov, Y. Hou, S. Hoogland, F. P. García de Arquer, E. H. Sargent, *Nat. Electron.* **2022**, *5*, 511.
[16] Z. Xu, X. Han, W. Wu, F. Li, R. Wang, H. Lu, Q. Lu, B. Ge, N. Cheng, X. Li, G. Yao, H. Hong, K. Liu, C. Pan, *Light: Sci. Appl.* **2023**, *12*, 67.
[17] Y. Fu, H. Zhu, J. Chen, M. P. Hautzinger, X. Zhu, S. Jin, *Nat. Rev. Mater.* **2019**, *4*, 169.
[18] B. Shi, P. Wang, J. Feng, C. Xue, G. Yang, Q. Liao, M. Zhang, X. Zhang, W. Wen, J. Wu, *Nano-Micro Lett.* **2023**, *15*, 3.
[19] Y. Zhang, Y. Ma, Y. Wang, X. Zhang, C. Zuo, L. Shen, L. Ding, *Adv, Mater* **2021**, *33*, 2006691.
[20] Y. Zhou, J. Luo, Y. Zhao, C. Ge, C. Wang, L. Gao, C. Zhang, M. Hu, G. Niu, J. Tang, *Adv. Opt. Mater.* **2018**, *6*, 1800679.
[21] L. Gao, K. Zeng, J. Guo, C. Ge, J. Du, Y. Zhao, C. Chen, H. Deng, Y. He, H. Song, G. Niu, J. Tang, *Nano Lett.* **2016**, *16*, 7446.
[22] X. Zhou, Z. Lu, L. Zhang, Q. Ke, *Nano Energy* **2023**, *117*, 108908.
[23] Z. Li, Z. Li, Z. Shi, X. S. Fang, *Adv. Funct. Mater.* **2020**, *30*, 2002634.
[24] X. Xing, T. Tong, M. Mohebinia, D. Wang, Z. Ren, V. G. Hadjiev, Z. Wang, J. Bao, *J. Phys. Chem. Lett.* **2022**, *13*, 6447.
[25] D. Zheng, T. Pauporté, *Adv. Funct. Mater.* **2024**, *34*, 2311205.
[26] I. López-Fernández, D. Valli, C. Wang, S. Samanta, T. Okamoto, Y. Huang, K. Sun, Y. Liu, V. S. Chirvony, A. Patra, J. Zito, L. De Trizio, D. Gaur, H. Sun, Z. Xia, X. Li, H. Zeng, I. Mora-Seró, N. Pradhan, J. P. Martínez-Pastor, P. Müller-Buschbaum, V. Biju, T. Debnath, M. Saliba, E. Debroye, R. L. Z. Hoye, I. Infante, L. Manna, L. Polavarapu, *Adv. Funct. Mater.* **2024**, *34*, 2307896.
[27] N. Ding, Y. Wu, W. Xu, J. Lyu, Y. Wang, L. Zi, L. Shao, R. Sun, N. Wang, S. Liu, D. Zhou, X. Bai, J. Zhou, H. Song, *Light: Sci. Appl.* **2022**, *11*, 91.
[28] Z. Xiao, Z. Song, Y. Yan, *Adv. Mater.* **2019**, *31*, 1803792.
[29] Z. Zhang, R. Zhao, S. Teng, K. Huang, L. Zhang, D. Wang, W. Yang, R. Xie, N. Pradhan, *Small* **2020**, *16*, 2004272.
[30] M. Zhang, J. Yan, J. Ma, X. Wang, T. Li, H. Jiang, X. Ji, M. Wang, R. Yang, Z. Liu, X. Qi, S. Cheng, X. Chen, Z. Shi, *Adv. Opt. Mater.* **2023**, *11*, 2203054.
[31] M. Yao, Q. Zhang, D. Wang, R. Chen, Y. Yin, J. Xia, H. Tang, W. Xu, S. Yu, *Adv. Funct. Mater.* **2022**, *32*, 2202894.
[32] K. Dong, H. Zhou, W. Shao, Z. Gao, F. Yao, M. Xiao, J. Li, Y. Liu, S. Wang, S. Zhou, H. Cui, M. Qin, X. Lu, C. Tao, W. Ke, G. Fang, *ACS Nano* **2023**, *17*, 1495.
[33] Z. Hu, B. Zhang, F. Zhang, X. Guo, Z. Lin, J. Zhang, Y. Hao, J. Chang, *Sci. China Mater.* **2023**, *66*, 3629.
[34] Y. Li, Z. Shi, L. Wang, Y. Chen, W. Liang, D. Wu, X. Li, Y. Zhang, C. Shan, X. S. Fang, *Mater. Horiz.* **2020**, *7*, 1613.
[35] S. Yan, Y. Kong, Z. Zhang, Z. Wu, Z. Lian, Y. Zhao, S. Su, L. Li, S. Wang, K. W. Ng, *ACS Appl. Mater. Interfaces* **2022**, *14*, 49975.
[36] R. Naheed, M. A. Zeb, K. Sabeeh, *Phys. Rev. B* **2024**, *109*, 115138.
[37] M. Liu, M. B. Johnston, H. J. Snaith, *Nature* **2013**, *501*, 395.
[38] S. Pammi, R. Maddaka, V. Tran, J. Eom, V. Pecunia, S. Majumder, M. Kim, S. G. Yoon, *Nano Energy* **2020**, *74*, 104872.
[39] C. Chen, Z. Li, L. Fu, *Light: Sci. Appl.* **2023**, *12*, 77.
[40] S. Han, J. Quan, D. Wang, H. Li, X. Liu, J. Xu, Y. Zhang, Z. Li, L. Wu, X. S. Fang, *Adv. Sci.* **2023**, *10*, 2206417.
[41] J. Ávila, C. Momblona, P. P. Boix, M. Sessolo, H. J. Bolink, *Joule* **2017**, *1*, 431.
[42] K. Dong, H. Zhou, Z. Gao, M. Xu, L. Zhang, S. Zhou, H. Cui, S. Wang, C. Tao, W. Ke, F. Yao, G. Fang, *Adv. Funct. Mater.* **2024**, *34*, 2306941.

[43] K. Dong, H. Zhou, M. Xiao, P. Gui, Z. Gao, F. Yao, W. Shao, C. Liu, C. Tao, W. Ke, G. Fang, *Appl. Phys. Lett.* **2022**, *120*, 191102.
[44] S. Wang, A. A. Khan, S. Teale, J. Xu, D. H. Parmar, R. Zhao, L. Grater, P. Serles, Y. Zou, T. Filleter, D. S. Seferos, D. Ban, E. H. Sargent, *Nat. Commun.* **2023**, *14*, 1852.
[45] K. Lu, M. Luo, W. Gao, Q. J. Wang, H. Sun, D. Nam, *Nat. Commun.* **2023**, *14*, 2580.
[46] W. Zhu, W. Zhen, R. Niu, K. Jiao, R. Zhang, L. Zhang, F. Xue, C. Zhang, *ACS Photonics* **2023**, *10*, 4465.
[47] Q. Guo, X. Qi, L. Zhang, M. Gao, S. Hu, W. Zhou, W. Zang, X. Zhao, J. Wang, B. Yan, M. Xu, Y. Wu, G. Eda, Z. Xiao, S. A. Yang, H. Gou, Y. Feng, G. Guo, W. Zhou, X. Ren, C. Qiu, S. J. Pennycook, A. T. S. Wee, *Nature* **2023**, *613*, 53.
[48] J. Yu, X. Kuang, J. Li, J. Zhong, C. Zeng, L. Cao, Z. Liu, Z. Zeng, Z. Luo, T. He, A. Pan, Y. Liu, *Nat. Commun.* **2021**, *12*, 1083.
[49] H. Long, H. Liu, X. Wang, B. Wang, R. Bai, Y. Yu, K. Xin, L. Liu, Y. Xu, J. Zhang, F. Jiang, X. Wang, Z. Wei, J. Yang, *Adv. Funct. Mater.* **2023**, *33*, 2306241.
[50] R. Loudon, *Adv. Phys.* **1964**, *13*, 423.
[51] J. Qin, H. Xiao, C. Zhu, L. Zhen, C. Xu, *Adv. Opt. Mater.* **2022**, *10*, 2201627.
[52] M. Yu, S. He, J. Liu, W. Li, M. Chen, D. Cheng, Y. Zhai, D. Shi, C. Kan, M. Jiang, *Appl. Phys. Lett.* **2024**, *124*, 243506.
[53] M. Yu, P. Wan, K. Tang, S. He, Q. Zhao, Y. Zhai, D. Shi, C. Kan, M. Jiang, *Surf. Interfaces* **2024**, *51*, 104627.
[54] F. Sun, H. Xu, W. Hong, Z. Sun, W. Liu, *Adv. Funct. Mater.* **2024**, *34*, 2313776.
[55] Z. Wang, R. Yu, C. Pan, Z. Li, J. Yang, F. Yi, Z. L. Wang, *Nat. Commun.* **2015**, *6*, 8401.
[56] L. E. MacKenzie, R. Pal, *Nat. Rev. Chem.* **2021**, *5*, 109.